

Low velocity shocks: signatures of turbulent dissipation in diffuse irradiated gas.

P. Lesaffre¹, G. Pineau des Forêts^{2,1}, B. Godard³, P. Guillard⁴, F. Boulanger², and E. Falgarone¹

¹ ENS, LERMA, UMR 8112, CNRS, Observatoire de Paris, 24 rue Lhomond 75005 Paris, France LRA/ENS

² Institut d'Astrophysique Spatiale (IAS), UMR 8617, CNRS, Université Paris-Sud 11, Bâtiment 121, 91405 Orsay Cedex, France

³ Departamento de Astrofísica, Centro de Astrobiología, CSIC-INTA, Torrejón de Ardoz, Madrid, Spain

⁴ Spitzer Science Center (SSC), California Institute of Technology, MC 220-6, Pasadena, CA 91125, USA

Received ...; accepted ...

Abstract

Context. Large scale motions in galaxies (supernovae explosions, galaxy collisions, galactic shear ...) generate turbulence, allowing a fraction of the available kinetic energy to cascade down to small scales before being dissipated.

Aims. We establish and quantify the diagnostics of turbulence dissipation in mildly irradiated diffuse gas in the specific context of shock structures.

Methods. We incorporate the basic physics of photon-dominated regions into a state-of-the-art steady-state shock code. We examine the chemical and emission properties of mildly irradiated ($G_0=1$) magnetised shocks in diffuse media ($n_H = 10^2$ to 10^4 cm⁻³) at low to moderate velocities (from 3 to 40 km.s⁻¹).

Results. The formation of some molecules relies on endoergic reactions. In J-shocks, their abundances are enhanced by several orders of magnitude for shock velocities as low as 7 km.s⁻¹. Otherwise most chemical properties of J-type shocks vary over less than an order of magnitude between velocities from about 7 to about 30 km.s⁻¹, where H₂ dissociation sets in. C-type shocks display a more gradual molecular enhancement as the shock velocity increases.

We quantify the energy flux budget (fluxes of kinetic, radiated and magnetic energies) with emphasis on the main cooling lines of the cold interstellar medium. Their sensitivity to shock velocity is such that it allows observations to constrain statistical distributions of shock velocities.

We fit various probability distribution functions (PDFs) of shock velocities to spectroscopic observations of the galaxy-wide shock in Stephan's Quintet (SQ) and of a Galactic line of sight sampling diffuse molecular gas in Chamaeleon. In both cases, low velocities bear the greatest statistical weight and the PDF is consistent with a bimodal distribution. In the very low velocity shocks (below 5 km.s⁻¹), dissipation is due to ion-neutral friction which powers H₂ low energy transitions and atomic lines. In moderate velocity shocks (20 km.s⁻¹ and above), the dissipation is due to viscous heating and accounts for most of the molecular emission. In our interpretation a significant fraction of the gas on the line of sight is shocked (from 4% to 66%). For example, C⁺ emission may trace shocks in UV irradiated gas where C⁺ is the dominant carbon species.

Conclusions. Low and moderate velocity shocks are important in shaping the chemical composition and excitation state of the interstellar gas. This allows to probe the statistical distribution of shock velocities in interstellar turbulence.

Key words. shock waves – astrochemistry – ISM: abundances – ISM: kinematics and dynamics – ISM: molecules

1. Introduction

Bulk motions in galaxies generated by e.g. supernovae explosions, galaxy collisions and galactic shear drive turbulence in the cold interstellar medium (ISM). A fraction of the available kinetic energy cascades down to smaller scales and lower velocities. This is spectacularly illustrated by the observations of the galaxy collision in Stephan's Quintet (SQ). The relative velocities of the galaxies (on the order of 1000 km.s⁻¹) would be expected to dissipate in high velocity shocks, thus creating a warm and hot plasma devoid of molecules. However, one observes that H₂ cooling is greater than the X-ray luminosity (Appleton et al. 2006; Cluver et al. 2010). This demonstrates that energy dissipation in the interstellar space involves an energy cascade and molecular gas cooling. Moreover, the H₂ ex-

citation diagram in SQ implies a distribution of temperatures much above the equilibrium temperature set by UV and cosmic ray heating. The same holds on much smaller scales in the case of the diffuse ISM in the Solar Neighbourhood (Gry et al. 2002; Ingalls et al. 2011). The range of gas temperatures can only be accounted for if the dissipation heats the gas through spatially localised events (Falgarone et al. 2005). This idea is also supported by observations of chemical species in the diffuse ISM such as CH⁺ and SH⁺ which cannot be reproduced by UV alone (Nehmé et al. 2008; Godard et al. 2012).

These dissipation processes have yet to be studied. Dissipative structures could take the form of e.g. shocks, vortices, current sheets, shear layers and most likely involve the magnetic field. This broad variety of processes, their different time

scales and therefore different impacts onto the global gas energetics and chemistry, call for simplified models to quantify observational diagnostics. Spectroscopy of molecular H_2 with Copernicus in the diffuse ISM motivated the first MHD shock models propagating in diffuse gas. These first models were also key to provide a first interpretation of CH^+ in the diffuse ISM (Mullan 1971; Draine et al. 1983; Flower et al. 1986; Gredel et al. 2002). ISO-SWS observations (Falgarone et al. 2005) of the pure rotational lines of H_2 in diffuse gas were also interpreted in the framework of mild turbulent dissipation (low velocity MHD shocks and/or velocity shears in small scale vortices). More recently, Godard et al. (2009) have modeled turbulent dissipation bursts in the diffuse ISM as vortices at very small scales and computed the chemical signatures they imprint on the gas.

In the present work, we use an updated version of the magnetised shock models of Flower & Pineau des Forêts (2003) to quantify composition and cooling lines for a range of shock velocities (from 3 to 40 km.s^{-1}) including very low velocities which were not thoroughly considered before. We compute grids of such shocks for two strengths of magnetic field and for three different densities. Our preshock conditions are representative of the cold diffuse ISM. Hence, we have incorporated the treatment of mild irradiation which includes UV heating but also impacts the chemistry through photo-ionisation and photo-dissociation.

The shock velocity can be a crucial parameter even at very low velocity. As it happens, the generation of molecules in the interstellar medium (ISM) is initiated by the formation of the H_2 molecule on dust grains surfaces. Then, the formation of more elaborate molecules relies on two main paths. First, one can add a proton to H_2 to form H_3^+ and then transfer the extra proton to a single atom (C, O, S and Si, with the notable exception of N). But H_3^+ is usually much less abundant than H_2 . Second, one can directly exchange an atom with one proton of the H_2 molecule. But these reactions are subject to energy barriers with high characteristic temperatures (such as 2980K in the case of the oxygen atom). Hence both paths are difficult and the observed molecular complexity of the ISM stands as a puzzle. Nevertheless, temperatures required to open the second path are obtained in low velocity shocks (7.5 km.s^{-1} is enough to reach 3000K). These shocks may therefore play an important role in shaping the molecular chemistry of the ISM.

The results of the present models may contribute to the interpretation of the observations of the full set of cooling lines of the cold neutral medium (CII, CI, OI, H_2 , CO and H_2O) in galaxies observed with the *Spitzer* and *Herschel* space telescopes. To illustrate this, we build models from statistical distributions of shock velocities which we compare to observed data in the SQ and in a line of sight in the Chamaeleon (Gry et al. 2002). We use our best fit models to discuss the impact of kinetic energy dissipation on the physical state and chemistry of the molecular gas in these two sources. We also make

predictions on other diagnostic lines to be observed with *Herschel*. We present the numerical method for our shock models in section 2, with the properties of our grid of shocks in section 3. In section 4, we use our results to interpret the H_2 -excitation diagram observed in SQ and Chamaeleon. We summarize and discuss our results in section 5.

2. Numerical method

The models we present in this paper are based on the plane-parallel steady-state shock code implemented in Flower & Pineau des Forêts (2003). We work from their version and include few more refinements mainly in order to deal with moderate irradiation.

2.1. Radiation

We start from the reactions network used in Flower & Pineau des Forêts (2003) and include the relevant photo-reactions. The photo-reactions have their rates of the form

$$R = \alpha G_0 e^{-\beta A_v} \quad (1)$$

where α and β are constants. We use an incident field equal to the standard interstellar radiation field (ISRF, Draine 1978), thus taking $G_0 = 1$. The extinction A_v is integrated along the model from the pre-shock where we use a value of $A_v = A_{v0} = 0.1$ which models extinction from the irradiation source by a “buffer” of matter. The value of A_{v0} is a parameter of the problem which selects how much mass is contained in this buffer. The local value for the extinction is then computed as

$$A_v = A_{v0} + \int_{x_0}^x dz \sigma_g n_H \quad (2)$$

where $\sigma_g = 5.34 \times 10^{-22} \text{cm}^3 \text{pc}^{-1}$ is the effective extinction per H nuclei column-density, n_H is the local density of H nuclei, x is the current position and x_0 is the position at the entrance of the preshock (ie: the point where we start our simulations). Our shocks are hence assumed to be irradiated “backward” compared to their direction of propagation. However this matters only a little because the total extinction through these shocks is small (on the order of $\Delta A_v = 0.01 (n_H/100 \text{cm}^{-3})$, where n_H is the pre-shock density). **This setup is in fact exactly similar to the one used by Bergin et al. (2004). However they focus on the properties of a uniform pressure photon-dominated region (PDR) following the shock, whereas we stop our computation right behind the shock, and they consider pre-shock densities of $n_H = 1 \text{cm}^{-3}$ much lower than ours.**

The reaction rates for the photo-dissociation of H_2 and CO include an additional factor f_{shield} to account for the shielding and self-shielding. We use the tables of Lee et al. (1996) for CO and Draine & Bertoldi (1996) for H_2 with a Doppler parameter

$$b_D = \sqrt{u_{\text{th}}^2 + u_{\text{turb}}^2} \quad (3)$$

where u_{th} is the thermal velocity of H_2 molecules and $u_{\text{turb}} = 1 \text{km.s}^{-1}$ accounts for microturbulence. However,

we neglect the effect of velocity gradients on the self-shielding. For instance:

$$R_{\text{H}_2+h\nu} = (2.54 \times 10^{-11} \text{s}^{-1}) f_{\text{shield}} e^{-6.3 A_v} \quad (4)$$

where

$$f_{\text{shield}} = \frac{0.965}{(1 + x/b_D)^2} + \frac{0.035 e^{-8.5 \times 10^{-4} \sqrt{1+x}}}{\sqrt{1+x}} \quad (5)$$

with $x = N(\text{H}_2)/(5 \times 10^{14} \text{cm}^{-2})$. Here, the quantity $N(\text{H}_2)$ is the column-density of H_2 molecules, computed as for the extinction:

$$N(\text{H}_2) = N_0(\text{H}_2) + \int_{x_0}^x dz n(\text{H}_2) \quad (6)$$

where $n(\text{H}_2)$ is the local density of H_2 molecules and $N_0(\text{H}_2)$ is the quantity of H_2 molecules in the ‘‘buffer’’ which shields the medium from the external radiation field. We match $N_0(\text{H}_2) \simeq 10^{20} \text{cm}^{-2}$ to $A_{v0} = 0.1$ by assuming this buffer is mainly molecular. Similarly we define $N_0(\text{CO})$ for the CO self-shielding but we use $N_0(\text{CO})=0$ as $A_{v0} = 0.1$ is usually well below the extinction at which CO is self-shielded in standard models of photon-dominated regions (PDR).

With this irradiation model, we integrated the chemical and thermal evolution of a fluid parcel with fixed density moving away from the radiation source at a constant velocity v_{PDR} where the subscript PDR refers to photon-dominated region. The resulting spatial profile (the trace of the thermal and chemical composition history of this fluid parcel along its path) corresponds to a steady PDR front moving towards the irradiation source at speed v_{PDR} . For very small velocities we recover a steady PDR front which compares quite satisfactorily to the Meudon PDR code (Le Petit et al. 2006) for $G_0 = 1$. **In the frame of this comparison** we switched off grains and PAHs reactions **in order to remain** closer to the Meudon PDR code setup. We note the PDR structure is insensitive to the choice of Lee et al. (1996) or Draine & Bertoldi (1996) for H_2 photo-dissociation. This is due to the fact that the rates differ only in regions where the absolute value of the rates are small, hence unimportant. For the same reason, we expect our results should poorly depend on the exact value of the above mentioned Doppler parameter b_D . Black & van Dishoeck (1987) also shows that this parameter is not crucial in PDRs.

Compared to Flower & Pineau des Forêts (2003), we refreshed the collision rates of OI by H atoms with the rates computed by Abrahamsson et al. (2007). These rates enter the computation of the atomic cooling due to O atoms. Atomic and molecular cooling are otherwise identical to those employed in Flower & Pineau des Forêts (2003). For instance, we use the molecular cooling rates tabulated in Neufeld & Kaufman (1993) for the cooling by CO and H_2O .

2.2. H_2 -excitation

We follow the time-dependent excitation of H_2 along the shock structure as in Flower & Pineau des Forêts (2003). Here, we include the treatment of the H_2 population for the 149 lowest energy levels. We check that this allows to compute the H_2 cooling accurately for shock velocities up to at least 40km.s^{-1} for the range of densities we consider in this work (see also Flower & Pineau des Forêts 2003).

| Parameter | Value | Comment |
|----------------------------|---------------------------------------|--|
| n_{H} | $10^2, 10^3$ or 10^4cm^{-3} | H nuclei pre-shock density |
| u | 3 to 40km.s^{-1} | Shock velocity |
| $b = B/n_{\text{H}}^{1/2}$ | 0.1 or 1 | Dimensionless magnetic field |
| A_{v0} | 0.1 | Buffer extinction |
| $N_0(\text{H}_2)$ | 10^{20}cm^{-2} | Buffer H_2 column-density |
| $N_0(\text{CO})$ | 0 | Buffer CO column-density |
| G_0 | 1 | External radiation field |
| ζ | $3 \times 10^{-17} \text{s}^{-1}$ | Nominal cosmic rays flux |
| OPR | 3 | Preshock H_2 ortho/para ratio |

Table 1. Values for the main physical parameters in our models.

We also use the knowledge of the population of the 8 lowest H_2 rotational levels to compute more accurately the rate of the reaction $\text{C}^+ + \text{H}_2$. To compute the rate state by state, we use Gerlich et al. (1987) (as in Agúndez et al. 2010, line 2 of table 1) for H_2 levels with $J = 0\dots 7$ and $v = 0$, and we use Hierl et al. (1997) (as in Agúndez et al. (2010), line 3 of table 1) for the other levels.

2.3. Grains

As in Flower & Pineau des Forêts (2003), we treat adsorption, collisional sputtering and collisional desorption of molecules from and onto grains. However, unlike them, we take pre-shock conditions without ice mantles.

As in Flower & Pineau des Forêts (2003) we account for the charge of grains by including all charge exchanges involving grains and electron detachment by **cosmic ray induced** secondary photons. The heating due to the photoelectric effect is included, however we discard the detachment of electrons due to the radiation field in the chemical network.

3. Grid of Models

3.1. Numerical protocole

For each value of our parameters described in the next section, we integrate the steady-state equations of multi-fluid MHD shocks (Flower et al. 1985; Heck et al. 1990) from entrance conditions at thermal and chemical equilibrium (see details of the pre-shock chemical conditions below). As stated above, we account for the changes in the properties of the irradiation field due to the increasing absorption as we penetrate deeper into the shock structure. The computation is stopped when the temperature decreases back to 20% above the temperature of the pre-shock.

3.2. Choice of parameters

We tune most of our parameters to the typical conditions encountered in the dilute interstellar gas in our galaxy. We list the main physical parameters of our model in table 3.2.

We specify indirectly the strength of the magnetic field transverse to the shock speed by using the **non-dimensional** parameter $b = (B/1\mu\text{G})/\sqrt{n_{\text{H}}/\text{cm}^3}$ which Crutcher et al. (2010) observe to take values from $b = 0.1$ to $b = 1$ for our range of densities. We later refer to these values by highly magnetized shocks for $b = 1$ and weakly magnetized shocks for $b = 0.1$.

| Element X | Fractional value $n(X)/n_H$ | | | PAHs |
|-------------|-----------------------------|-----------|-------------|----------|
| | total | gas | grain cores | |
| H | 1 | 1 | | 1.80(-5) |
| He | 0.1 | 0.1 | | |
| C | 3.56(-4) | 1.38(-4) | 1.63(-4) | 5.40(-5) |
| O | 4.42 (-4) | 3.02 (-4) | 1.40 (-4) | |
| N | 7.94(-5) | 7.94(-5) | | |
| Mg | 3.70(-5) | | 3.70(-5) | |
| Si | 3.70(-5) | 3.37(-6) | 3.37(-5) | |
| S | 1.86(-5) | 1.86(-5) | | |
| Fe | 3.23(-5) | 1.50(-8) | 3.23(-5) | |

Table 2. Elemental composition of the pre-shock gas (as in Godard et al. 2009). Initial conditions assume no ice mantles (bare cores). Note the gas to dust mass ratio is $\rho_{\text{gas}}/\rho_{\text{dust}} \simeq 180$. The numbers in the parentheses denote the powers of ten.

For both of these assumptions on the magnetic field, we build three grids of models, one for each pre-shock density between $n_H = 10^2 \text{ cm}^{-3}$, $n_H = 10^3 \text{ cm}^{-3}$ and $n_H = 10^4 \text{ cm}^{-3}$. **In the following, we will use the term *low velocity for shocks below 20 km.s⁻¹, moderate velocity above 20 km.s⁻¹ and high velocity at and above 40 km.s⁻¹*.** Each grid spans a range of velocities from 3 up to 40 km.s⁻¹ with a step of 0.5 km.s⁻¹, for an integration time of about 6 hours per grid on a typical workstation. We choose our minimum velocity of 3 km.s⁻¹ above the Alfvén speed in the neutral gas in the $b = 1$ case:

$$v_A = \frac{B}{\sqrt{4\pi\rho}} = \frac{b}{\sqrt{4\pi(\mu_H/\text{a.m.u.})}} = 1.85 b \text{ km/s} \quad (7)$$

where the mean mass per H nucleus is $\mu_H = \rho/n_H = 1.4 \text{ a.m.u.}$. We choose the upper bound of 40 km.s⁻¹ because of the limitations of our shock models¹.

At each fixed pre-shock density, we first evolve the gas chemically and thermally during 10^7 years, which brings the gas close to thermal and chemical equilibrium. We start with the same elemental abundances as in Godard et al. (2009), which are summarised in table 2. Note the gas phase abundance in the pre-shock is set to a tenth of the Si locked in the grains cores, **consistent with observations (Jenkins 2009)**. We also include PAHs with a fraction $n(\text{PAH})/n_H = 10^{-6}$ of the representative species $\text{C}_{54}\text{H}_{18}$. Without irradiation ($G_0 = 0$), PAHs influence the ionisation degree of the gas and the charge-ion coupling. However with mild irradiation (at $G_0 = 1$) it turns out that C^+ ions dominate the charge fluid and the role of PAHs is negligible. With our current irradiation parameters (G_0 , extinction and H_2 buffer), the atomic hydrogen fraction is $n(\text{H})/n_H = 7.9(-2)$, $1.3(-2)$ and $2.0(-3)$ in the preshock gas with respective densities $n_H = 10^2 \text{ cm}^{-3}$, 10^3 cm^{-3} and 10^4 cm^{-3} . We then use the resulting state as our pre-shock conditions to run the shock model for each velocity in turn.

3.3. C- and J-type shocks

Steady-state magnetized shocks in the interstellar medium are of one of two kinds: J-type shocks in which the ki-

¹ Indeed, the code does not treat doubly ionised species and radiative emission from the post-shock itself which might affect pre-shock conditions at high densities (see Flower & Pineau des Forêts 2010).

netic energy is dissipated viscously in a very sharp velocity *jump* (hence 'J') followed by a thermal and chemical relaxation layer and C-type shocks in which kinetic energy is *continuously* (hence 'C') degraded **into** heat and photons via ion-neutral friction and cooling. **Mullan (1971) was first to discover that high magnetic fields can transfer kinetic energy to thermal energy in a continuous manner and coined the term C-shock. Draine (1980), Draine et al. (1983), and Roberge & Draine (1990) then described the multifluid nature of these shocks. C-shocks occur as long as the shock velocity remains below the propagation speed of the magnetic precursor. This critical velocity above which a C-shock cannot exist is the magnetosonic velocity**

$$v_m = \sqrt{c_s^2 + v_{Ac}^2} \quad (8)$$

where $v_{Ac} = B/\sqrt{4\pi\rho_c}$ is the Alfvén speed in the *charged* fluid and c_s is the speed of sound. The Alfvén speed in the charges depends both on the magnetic field and on the inertia in the charged fluid. Thanks to the irradiation field, the gas is well ionised and provides ample free electrons to stick onto the grains. As a result most grains are charged **negatively** in our models and hence they dominate the inertia in the charged fluid. Moreover, Guillet et al. (2007) showed that even the neutral grains spend an extensive fraction of their time attached to the magnetic field and they should also be included in the charged fluid inertia. We hence include all PAH and grains in the computation of the magnetosonic speed. As a result, the Alfvén speed in the charged fluid v_{Ac} is larger than v_A by a factor $v_{Ac} \sim \sqrt{\rho/\rho_d} v_A$ where $\rho/\rho_d \sim 180$ is the gas to dust mass ratio. The actual number in *our* simulations turns out to be $v_m = 21.2 \text{ km.s}^{-1}$, 21.7 km.s^{-1} and 22.9 km.s^{-1} for respectively $n_H = 10^2 \text{ cm}^{-3}$, 10^3 cm^{-3} and 10^4 cm^{-3} in the case $b = 1$ and about ten times lower values for $b = 0.1$.

Shocks with speed greater than v_m will always be J-shocks. For instance, all shocks in our $b = 0.1$ grid are J-shocks. However, time-dependent shocks with velocities lower than v_m could be C-shocks, J-shocks or even a combination of the two (see Chièze et al. 1998; Lesaffre et al. 2004a,b). Indeed, **(i)** the transverse magnetic field could be lower for various orientations of the field (see Wardle 1998 for oblique C-shocks), **(ii)** or the C-shock could be at an earlier development of its structure where it still has a J-shock component (Chièze et al. 1998, Lesaffre et al. 2004a), **(iii)** or the final fate of the shock could be a steady-state CJ-shock depending on the history of the shock (Lesaffre et al. 2004a, Lesaffre et al. 2004b). As a result, we build our grids of models with C-shocks for shock velocities up to v_m and we use J-shocks for higher shock velocities. In the following, we explore the properties of the resulting shocks.

3.4. Weakly magnetized shocks ($b=0.1$)

For high compression ratios (ie: Mach numbers much greater than 1), the maximum temperature in a J-shock (obtained just behind the leading adiabatic shock front) is

$$T_{\text{max}} = \frac{2(\gamma - 1)}{(\gamma + 1)^2} \frac{\mu}{k_B} u^2 \quad (9)$$

where μ is the mean molecular weight of the gas, k_B is the Boltzman constant and u is **the shock velocity in the**

shock frame. Note the shock velocity is very close to the velocity difference between upstream and downstream gas for high Alfvénic Mach number. In particular, this relation shows that the peak temperature in a shock is proportional to the square of the shock velocity.

For such dilute molecular gas, only the lowest energy levels of H_2 are populated and the appropriate value for γ is $\gamma = 5/3$. With $\mu = 2.33$ a.m.u. (which corresponds to the above $\mu_H = 1.4$ in our near fully molecular conditions) relation (9) becomes:

$$T_{\max} = 53 \text{ K } (u/1 \text{ km.s}^{-1})^2. \quad (10)$$

Figure 1(a) displays the above theoretical value and the actual maximum temperature reached in our models for each velocity tested in our grid at $n_H = 10^2 \text{ cm}^{-3}$. Both values remain close to one another. At high temperature (high velocity), the maximum temperature is closer to the value obtained in equation (9) with $\gamma = 7/5$. This stems from the excitation of rotational levels of the H_2 molecules in the adiabatic front. Note that we use a viscous length $\lambda = 1/\sigma n_H$ with a viscous cross-section $\sigma = 3 \times 10^{-15} \text{ cm}^2$ based on H_2 - H_2 collision data computed by Monchick & Schaefer (1980) for a velocity dispersion of 1 km.s^{-1} . We checked that the viscous front between the peak temperature and the pre-shock is always adiabatic. Its width of 10^{13} cm , visible on Figure 1(b), corresponds to the viscous length for $n_H = 10^2 \text{ cm}^{-3}$. This figure surprisingly shows that higher velocity shocks return to pre-shock temperature on a smaller shock distance than low velocity shocks. However, the range of scales spans only one order of magnitude from $2 \times 10^{15} \text{ cm}$ down to $2 \times 10^{14} \text{ cm}$ with all shocks with velocities higher than 20 km.s^{-1} around the scale of $2 \times 10^{14} \text{ cm}$. Note that the range of flowing time through these shock structures also spans about one order of magnitude, from 400 yr to 2000 yr. For higher densities, the picture is much the same and in particular time scales vary little within one category (J-type or C-type) of shocks. However, shocks which strongly dissociate H_2 (such as dense shocks at moderate velocity) have a wide H_2 reformation plateau where H_2 reformation provides the necessary heat to keep the gas warm (Flower et al. 2003).

Figure 2(a) shows the total column-density of H nuclei (N_H) across each shock in the grid. Also displayed is the total H_2 column-density. The total N_H column-density is surprisingly constant around $N_H = 3\text{--}4 \times 10^{18} \text{ cm}^{-2}$ over the range of velocities in our grid except at both ends. The increase of the compression factor at higher shock speed is compensated by the shorter cooling length. This result is in contrast to the results obtained by Hollenbach & McKee (1989) in the velocity range 30 to 150 km.s^{-1} where the cooling column-density behind the shocks is seen to vary greatly. Shocks with velocities below about 7 km.s^{-1} have a lower than average total column-density, and shocks with velocities above 35 km.s^{-1} dissociate H_2 which decreases the amount of cooling and increases the total column-density.

Figures 2(b) and 2(c) show the total column-densities across the shock for various neutrals and ions. Remember the end of each shock is defined when the temperature decreases again under 20% above the pre-shock temperature. Since the overall column-density is a slowly varying function of the shock velocity (figure 2(a)) these plots also give a good estimate on how the average relative abundance of

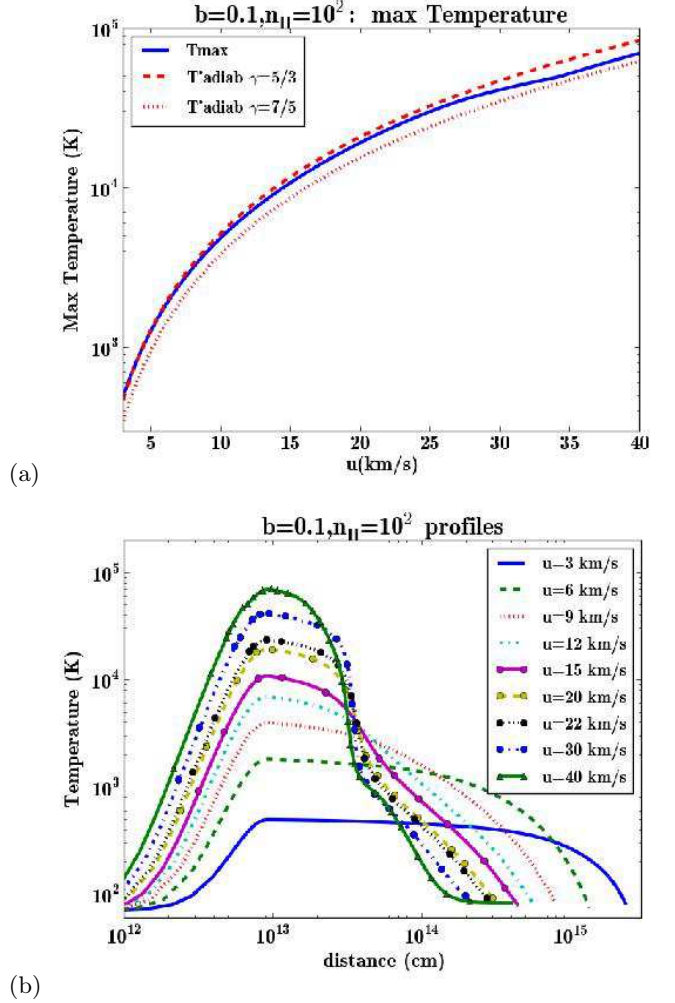


Figure 1. (a) Maximum temperature in the *weakly magnetized* shocks. (b) Temperature profiles for some representative *weakly magnetized* shocks, the fluid flows from left to right with the pre-shock on the left and the post-shock on the right. Only J-shocks are present for this low value of the magnetic field. $n_H = 10^2 \text{ cm}^{-3}$.

each of these species varies with respect to the shock velocity. One striking feature of these figures is the sharp rise of some molecular abundances at low velocity. We trace these apparent velocity thresholds to temperature barriers or endothermicities of key reactions which initiate the production of molecules. Equation (10) allows to relate these critical temperatures to key velocities in J-shocks. We list in table (3) the main bottleneck reactions which involve H_2 and a single atom or monoatomic ion along with their characteristic temperatures and J-shock velocities. At high velocities, the decrease in molecular content (around 35 km.s^{-1}) corresponds to the absence of H_2 molecules due to dissociation in the shock front.

Figure 2(c) illustrates the variation of a few ions of interest. The abundance of C^+ is controlled mainly by photoionisation of C and charge exchange with PAHs and H_2 . As the velocity increases, the post-shock density increases with enhanced charge exchange, thus decreasing the C^+ abundance. For very large velocities (above 35 km.s^{-1}) H_2

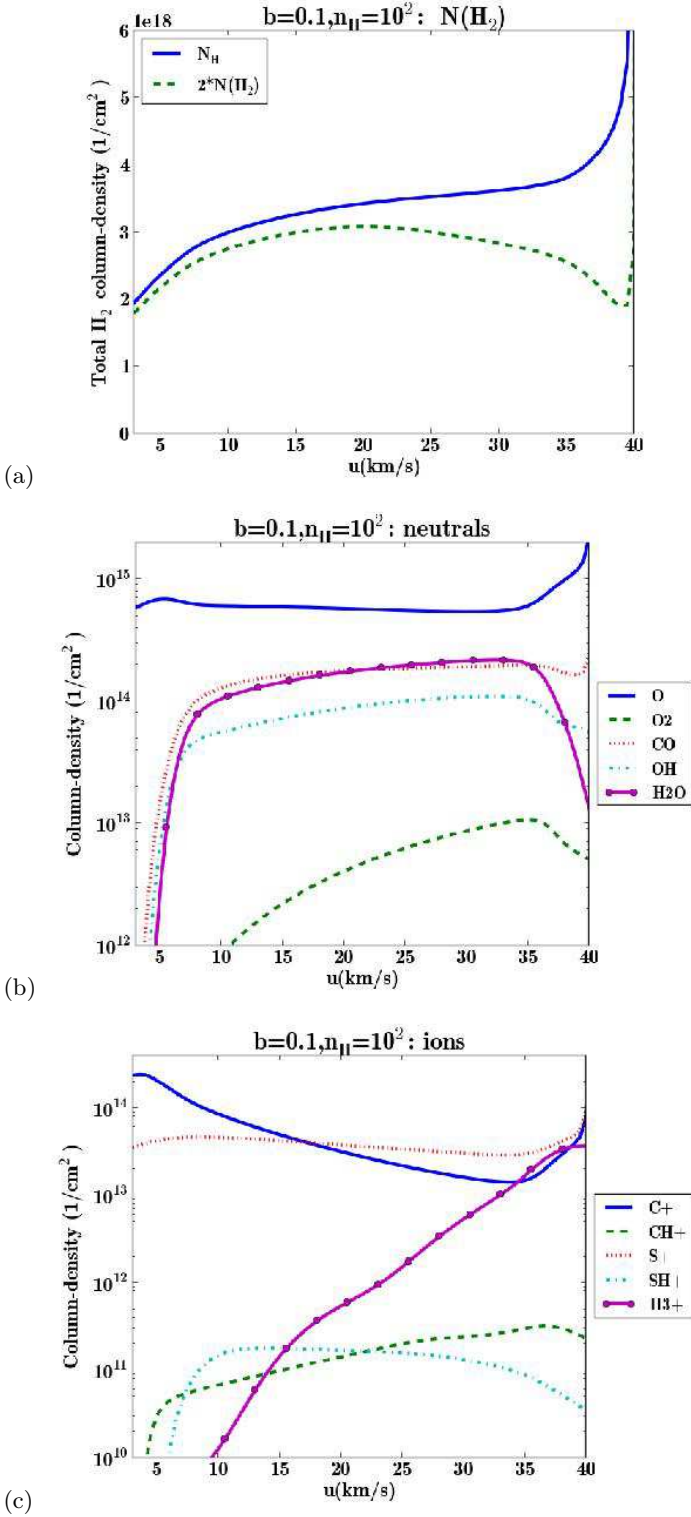


Figure 2. For each shock velocity in our *weakly magnetized* shocks ($b = 0.1$), we plot (a) the total H nuclei and H_2 molecules column-densities (b) some neutrals of interest and (c) some ions of interest. $n_{\text{H}} = 10^2 \text{ cm}^{-3}$.

starts to be dissociated and C^+ increases again. In a molecular medium, the abundance of H_3^+ is controlled by the balance between cosmic ray ionisation of H_2 (followed by a hydrogen exchange with H_2) and recombination of H_3^+ . The charge balance links the ionisation degree to the abundance

| Reaction | Temperature barrier | Velocity |
|--|---------------------|--------------------------|
| $\text{O} + \text{H}_2 \rightarrow \text{OH} + \text{H}$ | 2980 K | 7.5 km.s^{-1} |
| $\text{C}^+ + \text{H}_2 \rightarrow \text{CH}^+ + \text{H}$ | 4640 K | 9.4 km.s^{-1} |
| $\text{S} + \text{H}_2 \rightarrow \text{SH} + \text{H}$ | 9620 K | 13.5 km.s^{-1} |
| $\text{S}^+ + \text{H}_2 \rightarrow \text{SH}^+ + \text{H}$ | 9860 K | 13.6 km.s^{-1} |
| $\text{C} + \text{H}_2 \rightarrow \text{CH} + \text{H}$ | 14100 K | 16.3 km.s^{-1} |
| $\text{Si}^+ + \text{H}_2 \rightarrow \text{SiH}^+ + \text{H}$ | 14310 K | 16.4 km.s^{-1} |
| $\text{N} + \text{H}_2 \rightarrow \text{NH} + \text{H}$ | 14600 K | 16.6 km.s^{-1} |
| H_2 dissociation energy | 52000 K | 31.3 km.s^{-1} |

Table 3. List of bottleneck reactions for molecules formation with their temperature barrier or endothermicity and the corresponding velocity of the **J-type** shock that is able to provide such temperature computed using equation (10). $\text{N}^+ + \text{H}_2$ has little or no barrier: 168K.

of C^+ , thus the abundance of H_3^+ is inversely proportional to C^+ with an extra dependence on the square root of the temperature due to the temperature sensitivity of the recombination rate.

On figure 3 we display the variation of the total emission of various lines of interest depending on the shock velocities. This can be of interest for observers who want to characterize the velocities of observed shocks. Figure 3(a) shows some of the most observed atomic lines with the H_2 0-0S(1) line for comparison. The C^+ ion emission decrease at moderate velocities is an abundance effect. Atomic O cooling is enhanced at moderate velocities because these shocks dissociate H_2 : this slows down the cooling and yields a temperature plateau where O is the dominant cooling agent. The stronger the shock, the more time it takes for H_2 to reform, then the plateau widens and the O emission gets larger.

Figure 3(b) shows how the lowest energy lines of H_2 change with the velocity of the shock. The relative strengths of these lines vary greatly between $u=3 \text{ km.s}^{-1}$ and $u=10 \text{ km.s}^{-1}$. For example, the ratio S(1)/S(3) decreases from more than a hundred at 3 km.s^{-1} to about a fifth at 10 km.s^{-1} . Indeed, the shock peak temperature in this range of velocities spans the energies of the upper levels of these transitions ($J=7$ corresponds to 3474 K, for instance, and see figure 1(a) for how the maximum temperature in the shock varies with shock velocity): the excitation diagram in the low levels of H_2 is greatly affected in this range of temperatures. By contrast, the aspect of the excitation diagram does not change above 10 km.s^{-1} : the emissivities of these lines are unable to discriminate the shock velocity u for $u > 10 \text{ km.s}^{-1}$. Indeed, above 10 km.s^{-1} the temperature experienced in these shocks is much greater than the $J=7$ energy. Observers should use lines with upper levels with higher J values (such as rovibrational lines) to probe the velocities of these shocks or they should use diagnostics based on atomic lines.

On figure 4 we examine what fraction of the kinetic energy flux input

$$I_{\text{kinetic}} = \frac{1}{2} \rho u^3 \quad (11)$$

into the shock is radiated away by each coolant. Individual coolings are integrated through the whole shock structure as follows:

$$I_{\text{cool}} = \int_{x_0}^{x_1} \Lambda dz \quad (12)$$

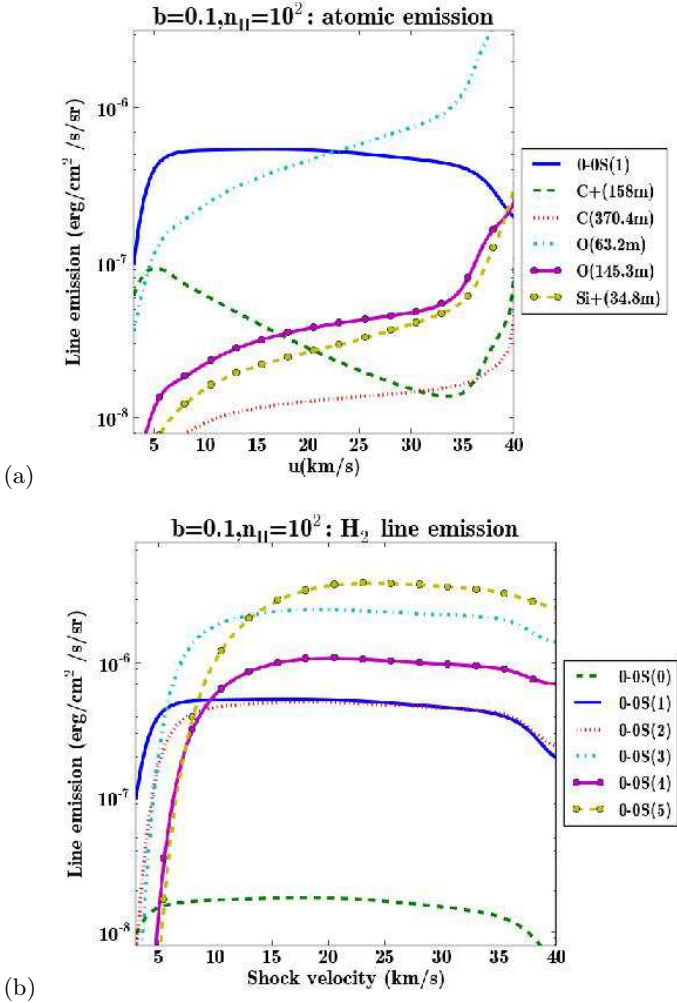


Figure 3. (a) Atomic and (b) pure rotational H_2 line emission for *weakly magnetized* shocks. $n_{\text{H}} = 10^2 \text{ cm}^{-3}$.

where Λ is the local rate of cooling and x_1 is the end point of the shock (ie: where the temperature decreases back to 20% above the pre-shock temperature). **We also display the magnetic energy flux across the shock**

$$I_{\mathbf{B} \text{ flux}} = \frac{B_e^2}{4\pi} u_i \quad (13)$$

where u_i is the ion velocity and B_e is the magnetic field at the end of the shock. H_2 cooling dominates almost everywhere except: (i) at very low velocity, where atomic O or C^+ cooling takes over depending on the density, and (ii) above the velocity for H_2 dissociation (which is lower for higher densities) where atomic O and H (Lyman- α) cooling take over. At density $n_{\text{H}} = 10^4 \text{ cm}^{-3}$, and below 20 km.s^{-1} , note that H_2O cooling becomes important.

3.5. Strongly magnetised shocks ($b=1$)

In a C-shock, the kinetic energy is continuously transformed into thermal energy via ion-neutral friction. As a result, the heating is spread out on a much larger region than for J-shocks and the peak temperature is hence much smaller as seen on figure 5(a). However, reactions between neutral and ion species benefit from the ion-neutral drift, and the

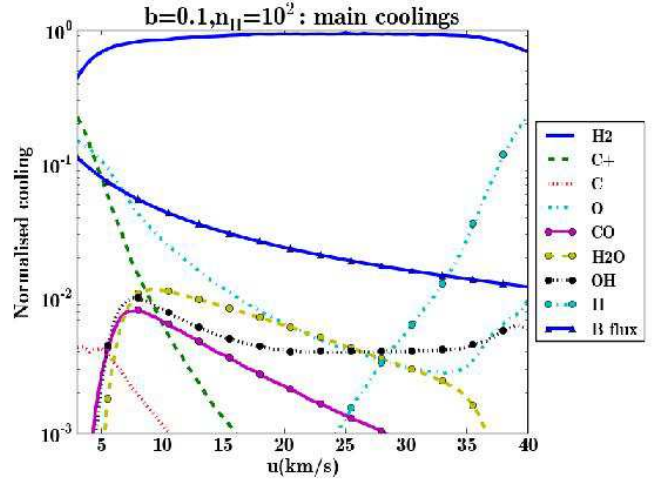


Figure 4. Cooling integrated along the shock length, normalised by kinetic power $\frac{1}{2}\rho u^3$ in *weakly magnetized* shocks, for $n_{\text{H}} = 10^2 \text{ cm}^{-3}$. The solid line with triangles shows the fraction of the power which is transferred into a flux of magnetic energy. On this figure, H_2 cooling incorporates the cooling from 200 lines between the 149 H_2 levels included in the simulation, whereas figure 3 considers only 6 individual lines amongst the lowest levels of H_2 .

effective temperature which is used to compute the reaction rate is higher (see Pineau des Forêts et al. 1986). For instance, the effective temperature for reactions involving C^+ and H_2 is

$$T_{\text{eff}}(\text{C}^+, \text{H}_2) \simeq \frac{2T_n + 12T_i}{2 + 12} + \frac{2 \times 12}{2 + 12} \frac{m_p}{3k_B} (u_n - u_i)^2 \quad (14)$$

where $(u_n - u_i)$ is the local drift velocity between the ions and the neutrals, m_p is the proton mass and T_n and T_i are respectively the temperatures of the neutral and ionised gas. Figure 5(a) shows the maximum effective temperature of the reaction $\text{C}^+ + \text{H}_2$, which incidentally is very close to the maximum temperature which would be obtained in the corresponding J-shock.

Compared to the temperature profile of a J-shock, the temperature profile of a C-shock is broad, with a lower temperature: see figure 5(b). However, within each type of shock, the total size of the shock structure varies over less than an order of magnitude for the range of velocities we tested, as is apparent on figure 5(b). This is even more striking for the flowing time scales across the shock structures which, for $n_{\text{H}} = 10^2 \text{ cm}^{-3}$, varies only from 8000 to 6000 years for the C-shocks and from 1500 to 1000 years for the J-shocks. As mentioned above, this holds for higher densities as well.

Slightly above 20 km.s^{-1} , all shocks in our grids of models are J-shocks, but the strength of the magnetic field varies from $b = 0.1$ in the previous subsection to $b = 1$ in this subsection. The higher magnetic field limits the compression in the shock and the collisional processes take longer to occur. In particular, the cooling length for the J-shocks above 20 km.s^{-1} is between $4 \times 10^{15} \text{ cm}$ and $7 \times 10^{15} \text{ cm}$: much wider than for the corresponding weakly magnetised J-shocks. The lower density but larger size of the shock impacts on the chemical composition and structure in subtle ways. A careful comparison of the right hand sides of figures

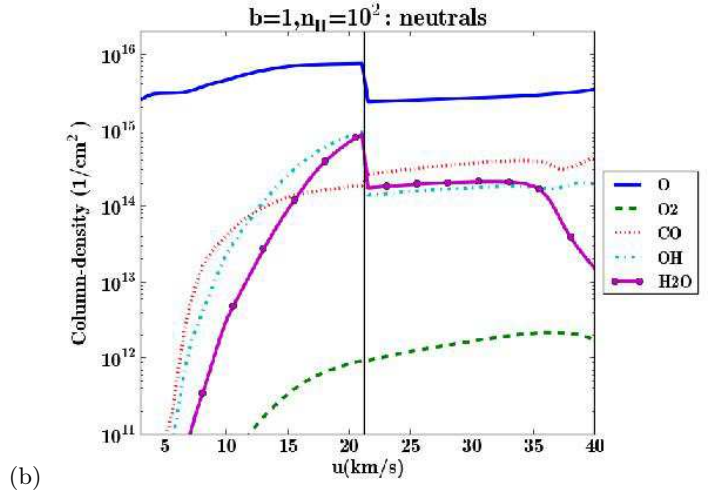
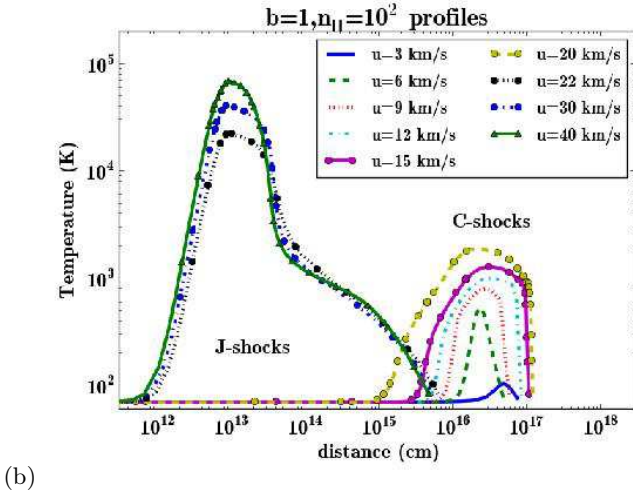
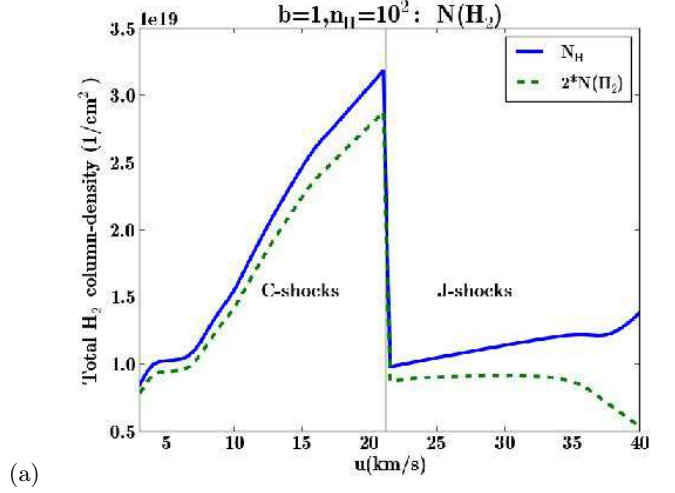
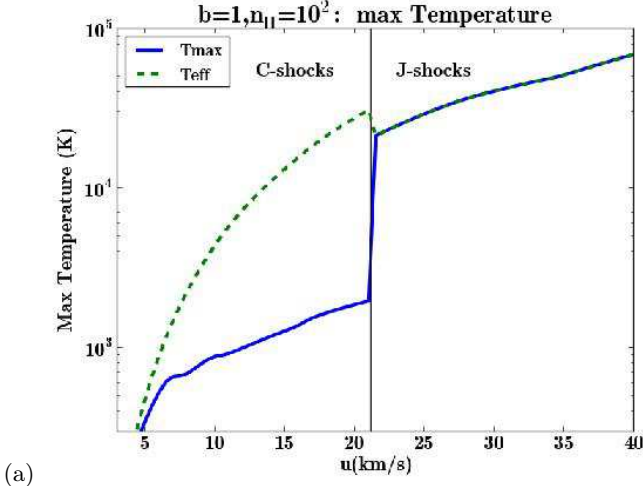


Figure 5. (a) Maximum temperature in the *highly magnetized* shocks (b) Temperature profiles for some representative *highly magnetized* shocks, the fluid flows from left to right with the pre-shock on the left and the post-shock on the right. $n_{\text{H}} = 10^2 \text{ cm}^{-3}$.

2 and 6 shows the column-density of H nuclei is higher in magnetised shocks and moderate variations in the chemical composition are noticeable.

Figure 6 shows the molecule production over the range of models in our grid at $n_{\text{H}} = 10^2 \text{ cm}^{-3}$. The transition from C-shocks (velocity lower than 21 km.s^{-1}) to J-shocks (higher shock speed) is clear. The column-densities of most species have a drop at 21 km.s^{-1} which expresses a boosted molecular production in C-shocks. Three effects are at play which favour molecules production in C-shocks.

First, the ion-neutral drift helps to overcome reaction barriers of ion-neutral reactions (which impact C-bearing species, for example, whose bottleneck reaction is $\text{C}^+ + \text{H}_2$). Second, the resulting frictional heating keeps the temperature warm throughout the shock. By comparison a J-shock is very hot at the peak temperature right behind the viscous front but quickly cools down in the trailing relaxation layer. Third, the steady frictional heating slows down cooling and compression in the relaxation layer and the net result is an increased total N_{H} column-density in C-shocks compared to J-shocks (see the drop at 21 km.s^{-1} in figure

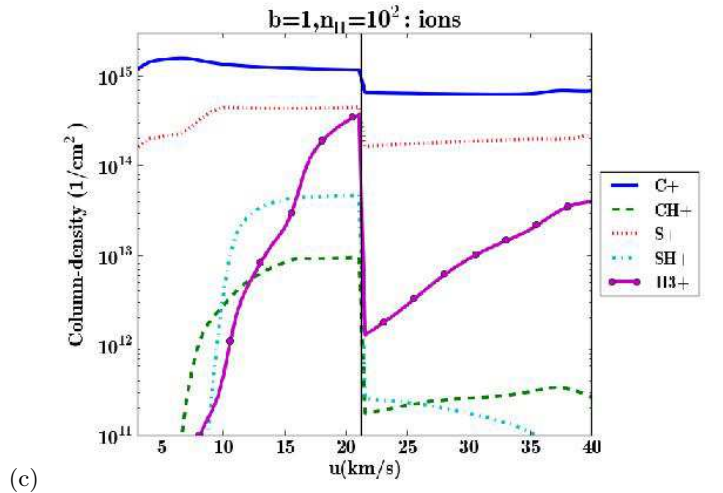


Figure 6. Same as figure 2 for *highly magnetized* shocks ($b = 1$). $n_{\text{H}} = 10^2 \text{ cm}^{-3}$.

6a). This is the main factor which impacts those molecular species whose production relies mainly on neutral-neutral reactions (such as O-bearing species). In particular, these species show a more gradual rise at low velocities, because of the slower rise of the maximum neutral temperature in C-shocks.

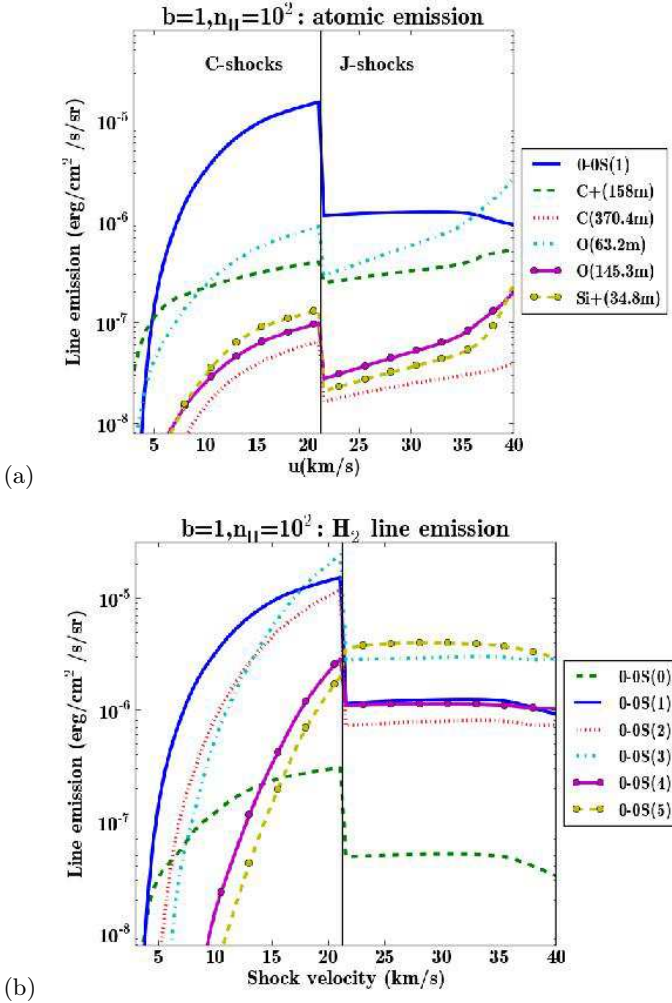


Figure 7. (a) Atomic and (b) rotational H₂ lines emission for highly magnetized shocks. $n_H = 10^2 \text{ cm}^{-3}$.

We display the total integrated emission in various lines of interest on figures 7(a) and 7(b): as for figure 3, these give clues on which observations constrain what shock velocity. In particular, the emissivities of H₂ lines with low J upper levels now vary from 3 to 20 km.s⁻¹, but are independent of velocity above 20 km.s⁻¹. The neutral temperature in C-shocks rises more slowly than J-shocks as shown by the comparison between figures 1 and 5, but the maximum temperature in C-shocks is more representative of the temperature in the whole mass of the shock and there is more column-density in C-shocks. As a result, the left hand sides (between 3 and 20 km.s⁻¹) of figures 7(a) and 7(b) look like blow ups of figures 3(a) and 3(b) shifted to greater emissivities. However, C⁺ stands out even more for C-shocks because its excitation benefits from the ion-neutral drift. The right hand sides of figures 7(a) and 7(b) are similar to the corresponding weakly magnetised J-shocks seen in figures 3(a) and 3(b): the emissivities are poorly affected by the density change due to the magnetic field except for C⁺.

In figure 8 we examine, averaged over the whole shock structure as in figure 4, what fraction of the kinetic energy flux input into the shock is radiated away by each coolant in the low density case ($n_H = 10^2 \text{ cm}^{-3}$). At very low ve-

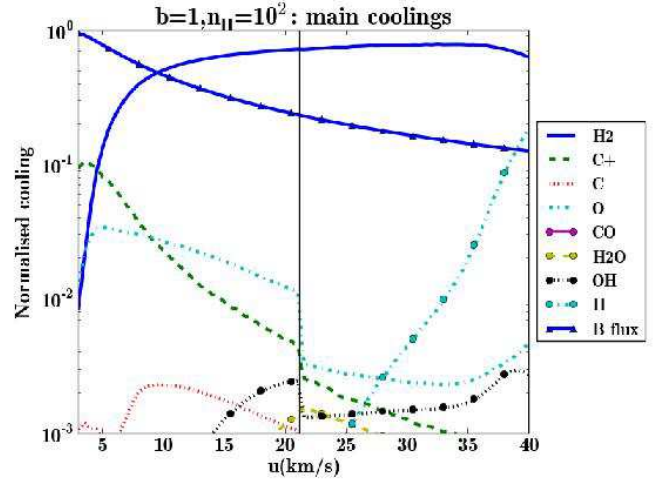


Figure 8. Cooling normalised by kinetic power in highly magnetized shocks for pre-shock density $n_H = 10^2 \text{ cm}^{-3}$. The solid line with triangles shows the fraction of the power which is transferred into a flux of magnetic energy.

locity, C⁺ is the most efficient coolant (rather than O for weakly magnetised shocks), but H₂ takes over for shock velocities shortly above 5 km.s⁻¹. Molecules such as CO, H₂O or OH carry less than a percent of this energy flux. The kinetic energy flux is mainly transferred into a magnetic energy flux (via field compression) for velocities below 10 km.s⁻¹ and is mainly radiated away above that velocity. At higher densities, the low velocity coolant becomes O. It is also interesting to note that at $n_H = 10^4 \text{ cm}^{-3}$ H₂O becomes an important cooling agent for low velocities. Flower & Pineau des Forêts (2010) also quoted the fraction of energy radiated away in various cooling processes in their shock models. However, in the present work the irradiation field photo-dissociates CO and ionises C so that C⁺ cooling is more prominent and CO cooling is less important than in their work, but the results are otherwise similar. In particular, they also find that the magnetic energy flux stores 50% of the injected power at $u = 10 \text{ km.s}^{-1}$.

4. PDF of shocks

4.1. Method of fit

Numerical simulations of driven supersonic turbulence show that the medium experiences a whole range of shock speeds: Smith et al. (2000) show that the probability distribution function (PDF) of the velocity jumps follows a decreasing power law with an exponential cut off at a Mach number of a few. Pety & Falgarone (2000) carefully separated vortical from compressional contributions in the velocity field of a compressible simulation of decaying supersonic turbulence: they uncover an exponential distribution for the convergence time scales $-1/\text{div}(v)$ where v is the fluid velocity. Subsonic wind tunnel experiments display an exponential distribution of velocity increments (Mouri et al. 2008).

These results hint at a variety of possible PDF shapes for the statistics of shocks, all favourably weighted towards low velocity shocks. Guillard et al. (2009) have modeled Spitzer H₂ observations of SQ with only two discrete values of the shock velocities. Here, we aim at fitting a statistical distribution of shocks to a collection

of observed quantities. Guided by the above remarks on turbulence, we fit various shapes of shocks PDF: decaying exponentials, power-laws, Gaussians and a piece-wise exponential fit.

We consider among $j = 1..M$ observable quantities an observable $X_j(u)$ associated to a steady shock of velocity u (expressed in km.s^{-1}). We note $f(u, \{p_i\}_{i=1..N})$ the probability density parametrised by the set of parameters $\{p_i\}_{i=1..N}$. Of course, the fitting makes sense only as long as the number of observed quantities M is sufficiently greater than the number of fitted parameters N . For example, an exponential PDF reads

$$f_e(u, p_1) = C(p_1) \exp(-p_1 u) \quad (15)$$

with the normalisation constant

$$C(p_1) = 1 / \sum_{u \geq 3}^{u \leq 40} \exp(-p_1 u). \quad (16)$$

We then compute observable quantities averaged over the PDF of shocks as

$$\bar{X}_j(\{p_i\}_{i=1..N}) = \sum_{u \geq 3}^{u \leq 40} X(u) f(u, \{p_i\}_{i=1..N}). \quad (17)$$

In order to ease the fitting process, we normalise the above values to the sum of the observable quantities:

$$\hat{X}_j = \frac{\sum_{j=1..M} X_j^0}{\sum_{j=1..M} \bar{X}_j} \bar{X}_j \quad (18)$$

where $\{X_j^0\}_{j=1..M}$ are the actual observed values. Note that this normalisation renders irrelevant the normalisation constant of each PDF, but it decreases by one unit the number of degrees of freedom $M_{\text{free}} = M - N - 1$. We finally find the optimal set of parameters $\{p_i^0\}_{i=1..N}$ which minimises the quantity

$$\chi^2(\{p_i\}_{i=1..N}) = \frac{1}{M_{\text{free}}} \sum_{j=1..M} \left(\log_{10} \hat{X}_j - \log_{10} X_j^0 \right)^2 / W_j^2$$

where W_j is the uncertainty on the observed value $\log_{10} X_j^0$. We also retrieve estimates $\{E_i\}_{i=1..N}$ of the errors on the parameters by computing the diagonal elements of the covariance matrix of $\frac{\partial^2}{\partial p_i^2} \chi^2$ on the optimal set.

Table 4 summarises the various PDFs we tried and their parametrization. The exponential and power-law PDFs are motivated by the above mentioned work on the statistical distribution of shocks in numerical and laboratory experiments. The piece-wise exponential PDF is built on intervals designed such that the observable quantities vary significantly (cf. figures 3 and 7). Otherwise, the parameters would be degenerate. We use as parameters the PDF value at the transition between these intervals. Thus, these parameters' optimal values and corresponding error bars directly probe the PDF and its uncertainty at these chosen locations. Finally, we use a single or a double Gaussian PDF to mimic the fit of one shock or two independent shocks: this allows to connect with the work of Guillard et al. (2009).

In addition, we note that the choice of the boundaries (upper and lower velocities) for the range of our grid of models does not affect significantly our results. This stems

| PDF | formula | N |
|------------------------|---|---|
| Power-Law | u^{-p_1} | 1 |
| Exponential | $\exp(-p_1 u)$ | 1 |
| Piece-wise exponential | at $u = 3, 10, 20, 40$ $f(u) = 1, p_1, p_2, p_3$ | 3 |
| 1-Gaussian | $e^{-(u-p_1)^2}$ | 1 |
| 2-Gaussian | $e^{-(u-p_1)^2} + p_3 e^{-(u-p_2)^2}$ | 3 |

Table 4. Template PDFs adjusted to the observed data (normalisation constants are discarded as irrelevant, see text).

from the fact that the shock emission is very small at low velocity and high velocity shocks are very rare in the solutions we obtain. Finally, grids of models with velocity spacings of 1 km.s^{-1} and 0.5 km.s^{-1} gave similar results, which validates the resolution we chose.

4.2. Applications

4.2.1. The Stephan's Quintet galaxy collision

In this section we use our model results to fit H_2 line emission from the galaxy-wide shock in SQ. This shock structure, first identified in radio continuum observations and X-ray images, was discovered to be a luminous H_2 source with *Spitzer* (Appleton et al. 2006; Cluver et al. 2010). It is associated with the entry of a galaxy into a group of interacting galaxies with a relative velocity $\sim 1000 \text{ km.s}^{-1}$. The luminosity of the molecular gas in H_2 rotational lines is observed to be larger than that of the plasma in X-rays. Guillard et al. (2009) present a first interpretation where the H_2 emission is powered by dissipation of turbulence driven by the large scale collision. CO observations have since shown that the kinetic energy of the molecular gas is larger than the thermal energy of the hot (X-ray emitting) plasma. It is the main energy reservoir available to power the H_2 line emission (Guillard et al. 2012). Guillard et al. (2009) show that the H_2 excitation is well fit by a combination of two MHD shocks with velocities of 5 and 20 km.s^{-1} in dense gas ($n_{\text{H}} \sim 10^3$ to 10^4 cm^{-3}), using the shock models of Flower & Pineau des Forêts (2003), which do not take into account UV radiation. Our grid of models allows us to test an alternative interpretation where the H_2 emission is accounted for with MHD shocks in lower density UV irradiated gas. In doing so we quantify a solution where the physical state of the H_2 gas in SQ is akin to that of the cold neutral medium in the Galaxy. Evidence that the gas is magnetized comes from radio continuum observations. The synchrotron brightness of the shock yields a magnetic field value $B \sim 10 \mu\text{G}$, assuming equipartition of magnetic and cosmic-ray energy (Xu et al. 2003). This value is comparable to the field strength reported by Crutcher et al. (2010) for the Galactic diffuse ISM. The mean UV radiation field in the SQ shock estimated to be $G_0 = 1.4$ (Guillard et al. 2010), is also close to the reference value for the ISM in the Solar Neighborhood.

The wide extension (30 kpc) of the SQ shock suggests that in the relaxation layer which follows the main high velocity ($\sim 600 \text{ km.s}^{-1}$) shock, a large number of sub-structures are formed which then collide and yield a range of sub-shocks with much smaller velocities (see Guillard et al. 2009). Simulations of large scale shocks subject to ther-

mal instability indeed show that turbulence is sustained in the trailing relaxation layer (Koyama & Inutsuka 2002 and later Audit & Hennebelle 2005; Hennebelle & Audit 2007; Audit & Hennebelle 2010). This connects with the theoretical work on turbulence mentioned above, and justifies our investigation with continuous PDFs of shock velocities. The observable targets which we aim at reproducing are the emission values for the six H₂ lines 0-0 $S(0)$ to $S(5)$ in table 1 of Cluver et al. (2010) which are integrated over the main shock structure.

Table 5 shows the best χ^2 obtained in all our attempts to fit the data. Two solutions stand out with χ^2 values reasonably close to one, namely: the piece-wise exponential and the two Gaussians at $b = 1$ and $n_{\text{H}} = 10^2 \text{ cm}^{-3}$ (their χ^2 values are emphasised in bold faces in table 5). Figure 9 illustrates the quality of the fit on the observed H₂-lines. Our models reproduce quite accurately every H₂-line except for 0-0 $S(4)^2$. For comparison, when we use the same technique and same grid of models as Guillard et al. (2009) (ie: models without irradiation at $n_{\text{H}} = 10^4 \text{ cm}^{-3}$), we find the best fit is obtained for two shocks of velocity 5 and 22 km.s⁻¹ in proportion 1:0.008 with a reduced $\chi^2 = 78$ (compared to $\chi^2 = 15.8$ for velocities 3.7 and 21 km.s⁻¹ in proportion 1:0.0002 in our 2-Gaussians high-density case). The coincidence of the optimal parameters with our 2-Gaussian solution is surprising, but the improvement on the χ^2 in the present work is also striking. Irradiation does really improve the comparison with the observations. Our work also shows that low-density solutions are even more viable than the previously found high-density solutions.

All optimal PDF shapes we find (including those with a large χ^2) are statistically biased towards low velocity shocks. Figure 10 displays the two best fit PDF solutions. The error bars (gray regions in these figures) are determined as follows: we vary the parameters of the PDFs at the extreme of their 3- σ range of uncertainty and we take the minimum and maximum values predicted when using these extreme PDFs. The piece-wise exponential adjustment shows a dip at 10 km.s⁻¹ which indicates a bimodal distribution of shocks consistent with the two-Gaussian fit (which is bimodal in essence...). Perturbation tests of this fit show that the PDF level at 10 km.s⁻¹ depends mainly on the ratio $S(0)/S(1)$, with a deeper dip for higher values of this ratio. On the other hand, the currently observed data do not discriminate whether the distribution of moderate velocity shocks is wide spread or well centred on a distinct velocity. Indeed, as seen on figure 7(b), above 20 km.s⁻¹ the emission properties of the observed H₂ lines do not change with velocity, hence these lines cannot probe the shape of the PDF in this range of velocities. Ro-vibrational lines should be used to probe the shocks at these velocities. We note all piecewise-exponential solutions (including those with a larger χ^2 at higher densities) are similarly consistent with bimodal distributions. This is not expected from the statistics of shock velocities in numerical simulations of turbulence. It may be a result of the intrinsic multiphase nature of the interstellar medium, where the moderate velocity shocks would be interpreted as collisions between molecular clouds and low velocity shocks would be the signature of turbulence dissipation within these clouds.

² This line actually lies at the position of the 7.7 μm PAH emission feature, which makes it difficult to measure accurately.

For each of the optimal PDF found, we can predict the value \hat{X} of other quantities of interest. We provide in table 6 the total column densities for some molecules and the expected emission of some atomic lines in our best two solutions. **These total column-densities are integrated from the pre-shock to the point where the temperature decreases back to 20% above the pre-shock temperature.** In particular, we provide a measure of the total H₂ column-density: the piece-wise exponential model yields

$$N_{\text{shocked}}(\text{H}_2) = 2.6 \times 10^{20} \text{ cm}^{-2}$$

and the 2-Gaussian model yields

$$N_{\text{shocked}}(\text{H}_2) = 1.0 \times 10^{20} \text{ cm}^{-2}.$$

Recent measurements from CO spectroscopy (Guillard et al. 2012) allow to estimate the total H₂ column-density in the SQ large scale shock structure as

$$N_{\text{total}}(\text{H}_2) = 8.5 \times 10^{20} \pm 1.5 \times 10^{20} \text{ cm}^{-2}$$

(assuming a Galactic value for the CO emission to H₂ column conversion factor). This puts the fraction of shocked gas in this line of sight between 32% and 12%, depending on which model we adopt, which confirms the results of Guillard et al. (2010) that quite substantial amounts of gas are shock-heated. In fact, quite a few of our optimal solutions predict $N_{\text{shocked}}(\text{H}_2) > 10^{21} \text{ cm}^{-2}$ and are therefore probably ruled out (only the viable solutions are underlined in table 5).

Since the shocks account for a significant fraction of the gas mass, any chemical enhancements in the shocks may have a significant contribution to molecular abundances. Table 6 also gives estimates of the chemical yields in these shocks. For example, the H₂O abundance is on the order of 10⁻⁶, significantly greater to that observed in the diffuse ISM in the Milky-Way (Wyrowski et al. 2010). These abundances could be even higher if the medium is clumped (and therefore shielded) and *Herschel* may provide a good opportunity to test this. For standard irradiation C⁺ is the dominant carbon gas species and this is also a result which will depend on shielding.

The importance of these species (in addition to H₂), as cooling agents of the interstellar turbulence depends directly on their abundance. *Herschel* observations could thus provide additional constraints to achieve a precise modelling of the physical and chemical state of the gas. We provide estimates of the total integrated flux in the molecular cooling agents in table 6: H₂ itself is responsible for more than 94% of the cooling in both our best-fit models. However its emission is distributed over many different lines, the strongest of which H₂-S(1) contributes by a few percent of the total. Note that for low-velocity C-shocks the pure rotational lines sum up to almost all the H₂ cooling. On the contrary, moderate velocity J-shocks experience much higher temperatures and the energy in these shocks is radiated away through higher H₂-levels. If our models with a contribution from moderate velocity J-shocks hold, a lot more energy should be emitted from higher excitation levels of the H₂ molecule than is observed from pure rotational lines. Finally, note that other molecular coolants contribute at most a few percent of the H₂-S(1) luminosity.

The emission of the C⁺ line at 158 μm is quite strong in our best two models (about half as strong as the H₂-S(1)

| b | n_{H} | 1-Gauss | pow-law | exp. | pw-exp. | 2-Gauss |
|-----|----------------|--------------|---------------|-------|--------------|-------------|
| 0.1 | 10^2 | <u>371.8</u> | 2307.0 | 54.3 | <u>60.8</u> | 11.2 |
| 0.1 | 10^3 | <u>504.0</u> | 1650.4 | 152.4 | <u>61.1</u> | 105.6 |
| 0.1 | 10^4 | <u>416.1</u> | <u>2139.9</u> | 174.3 | <u>580.8</u> | 155.3 |
| 1 | 10^2 | 1628.5 | <u>184.2</u> | 598.5 | 2.6 | 2.0 |
| 1 | 10^3 | 139.3 | 175.1 | 35.9 | <u>5.0</u> | <u>13.8</u> |
| 1 | 10^4 | 130.3 | 1648.0 | 12.6 | 6.3 | <u>15.8</u> |

Table 5. Summary of the optimal χ^2 values obtained in all our attempts to fit the SQ data. Both our optimal values are emphasised in bold faces. n_{H} is given in cm^{-3} . Underlined values correspond to solutions which have $N(\text{H}_2) \leq 10^{21} \text{cm}^{-2}$.

line), and so is the OI emission to a lesser extent. Assuming all carbon is in the form of C^+ in the un-shocked fraction of the total line of sight column-density $N_{\text{total}}(\text{H}_2)$, we predict that the C^+ line should shine about as much as the $\text{H}_2\text{-S}(1)$ line, with a significant contribution from shocks (66% and 52% respectively in both models). **Interestingly, this was also suggested in an interpretation of AKARI observations by Suzuki et al. (2011).** In contrast, the model proposed by Guillard et al. (2009) with no UV irradiation has no CII emission. This means that C^+ can indeed be a good signature for the dissipation of kinetic and magnetic energy in weakly shielded gas (as previously found by Falgarone et al. 2007). We also note that our viable models at higher densities predict even stronger emission in C^+ by up to a factor of three. As such, C^+ emission measurements will help to probe both the density and shielding of the gas. **By contrast to C^+ , the measured emission of the Si^+ line at $34.8 \mu\text{m}$ is much greater than the predicted emission from our shock models. It is probably dominated by the contribution from the hot ionised medium, as already suggested by Cluver et al. (2010).**

Figure 11 displays the distribution of energy radiated away for several cooling agents in the best-fit 2-Gaussian solution. A significant fraction of energy is dissipated in low-velocity shocks but more energy is radiated within moderate velocity shocks. Indeed the dissipated power goes as the cube of the velocity, which slightly more than compensates the higher number of low-velocity shocks. The figure clearly demonstrates that H_2 is by far the main cooling agent. It also shows that the emission from atomic cooling agents comes mainly from low-velocity shocks whereas the molecular emission is dominated by moderate velocity shocks. Similarly, we have checked that the emission from low J H_2 -lines probe low-velocity shocks whereas higher J lines probe larger velocity shocks, which seems rather natural.

4.2.2. Chamaeleon

Nehmé et al. (2008) successfully interpreted observational results of a line of sight **sampling diffuse molecular gas in front of the star HD 102065 in Chamaeleon**. Their PDR model with $G_0 = 0.4$, $n_{\text{H}} = 80 \text{cm}^{-3}$ and $A_v = 0.67$ reproduced accurately as many as seven independent observational quantities. However, they were unable to account for the column-densities of rotationally excited states of H_2 and failed to reproduce the observed abundance of CH^+ . Here, we assume that both a PDR and a statistical distribution of shocks contribute to this line of sight. Hence we

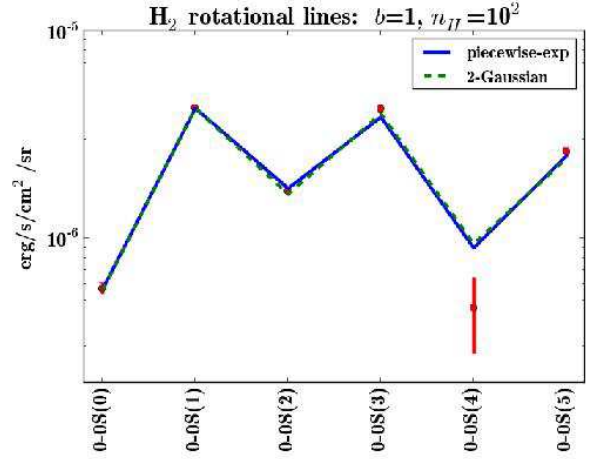


Figure 9. Observed fluxes of the H_2 lines in the SQ (red dots with error bars: Cluver et al. 2010, see also table 6) with the results of our best two models. **Note most error bars are so small they remain barely visible.**

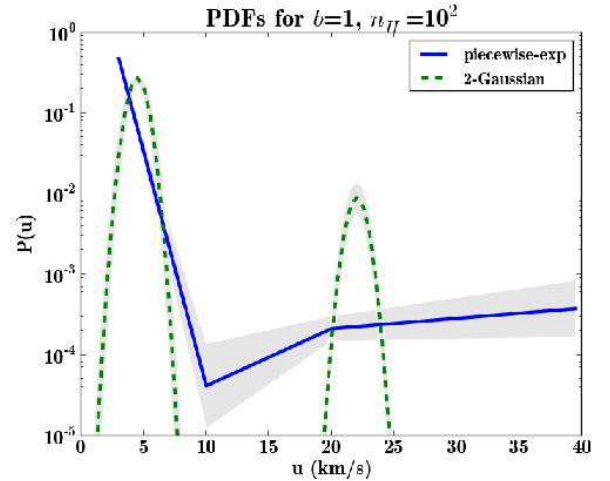


Figure 10. Shape of our best two optimal PDFs fit to the SQ data. Grey areas represent uncertainties due to the propagation of observational errors (see details in text).

attempt to fit as many as 11 observational measurements available for this line of sight with a linear combination of our shock models and a PDR model.

The PDR model is computed with our shock code in a PDR mode, see section 2.1. In principle, we should fit all irradiation parameters of the PDR alongside the grid of shocks. But this would assume we recompute the whole grid of shocks each time we probe new irradiation parameters and would lead to prohibitive computational time. Hence we fixed the irradiation conditions and the PDR model therefore introduces only one extra parameter in the fit: its weight in the line of sight compared to the shock models. We use $G_0 = 4$ and $A_v = 0.335$ as entrance conditions for both the PDR and the shocks and we compute a new grid of shock models from 3 to 40 km.s^{-1} with $n_{\text{H}} = 80 \text{cm}^{-3}$ and an ortho/para ratio of 0.7 as is observed.

We thus obtain reasonable χ^2 values with a best value of 11 for both the 2-Gaussian and the piecewise-exponential.

| name | pw-exp | 2-Gauss | obs. | err. |
|---|---------|---------|----------|---------|
| H ₂ -lines observations (erg.cm ⁻² .s ⁻¹ .sr ⁻¹) | | | | |
| 0-0S(0) | 5.7(-7) | 5.6(-7) | 5.8(-7) | 3.5(-8) |
| 0-0S(1) | 4.2(-6) | 4.2(-6) | 4.3(-6) | 4.8(-8) |
| 0-0S(2) | 1.7(-6) | 1.7(-6) | 1.7(-6) | 7.0(-8) |
| 0-0S(3) | 3.8(-6) | 4.0(-6) | 4.2(-6) | 1.5(-7) |
| 0-0S(4) | 9.0(-7) | 9.4(-7) | 4.7(-7) | 1.8(-7) |
| 0-0S(5) | 2.5(-6) | 2.4(-6) | 2.6(-6) | 1.3(-7) |
| Predictions | | | | |
| Column-densities (cm ⁻²) | | | | |
| H ₂ (0,0) | 5.8(19) | 2.2(19) | - | - |
| H ₂ (0,1) | 1.8(20) | 7.6(19) | - | - |
| H ₂ (0,2) | 3.4(18) | 3.4(18) | - | - |
| N(H ₂) | 2.5(20) | 1.0(20) | <1.0(21) | - |
| N(H) | 4.3(19) | 1.8(19) | - | - |
| N(C ⁺) | 7.6(16) | 3.2(16) | - | - |
| N(CO) | 2.5(14) | 1.8(14) | - | - |
| N(H ₂ O) | 1.6(14) | 1.9(14) | - | - |
| N(OH) | 1.9(14) | 1.7(14) | - | - |
| N(CH) | 2.1(13) | 1.0(13) | - | - |
| N(CH ⁺) | 1.7(12) | 1.1(12) | - | - |
| N(HCO ⁺) | 7.4(11) | 6.2(11) | - | - |
| Atomic lines (erg.cm ⁻² .s ⁻¹ .sr ⁻¹) | | | | |
| S(25.2m) | 1.4(-8) | 7.0(-9) | - | - |
| Si+(34.8m) | 9.8(-8) | 7.9(-8) | 1.6(-6) | 5(-8) |
| O(63.2m) | 1.4(-6) | 9.5(-7) | - | - |
| O(145.3m) | 1.2(-7) | 9.0(-8) | - | - |
| C+(158m) | 3.4(-6) | 2.2(-6) | - | - |
| C(370.4m) | 4.6(-8) | 3.1(-8) | - | - |
| C(609.8m) | 2.2(-8) | 1.3(-8) | - | - |
| Integrated molecular cooling (erg.cm ⁻² .s ⁻¹ .sr ⁻¹) | | | | |
| E(H ₂) | 1.6(-4) | 5.4(-5) | - | - |
| E(CO) | 4.4(-8) | 2.9(-8) | - | - |
| E(H ₂ O) | 1.1(-7) | 1.0(-7) | - | - |
| E(OH) | 4.1(-7) | 1.0(-7) | - | - |

Table 6. Results of our best two fits to the observed spectral line energy distribution in the SQ (flux are given in erg.cm⁻².s⁻¹.sr⁻¹) and their respective predictions: column-densities are in cm⁻² and cooling is indicated in erg.cm⁻².s⁻¹.sr⁻¹. **Parentheses denote powers of ten.**

The error mainly comes from overestimating the column-density in $J = 5$, but the molecular chemistry of the line of sight is reproduced rather accurately (see table 7).

The best two fitting PDFs compare qualitatively well to the solutions we found for SQ, except the low velocity part of the 2-Gaussian is more tightly peaked on low velocities (the moderate velocity component accounts for 3% of the total probability), and the piecewise-exponential dip at 10 km.s⁻¹ is less pronounced. The two PDF shapes are hence slightly less consistent than for the SQ, and continuous solutions are not ruled out (the exponential and power-law solutions yield χ^2 values on the order of 20 and 15 respectively). However, in the case of the Chamaeleon, the physical extent of the measured beam is much smaller than for the SQ. In particular, the total number of shocks involved is presumably much smaller and discrete numbers effects might show up in the distribution.

Our best two models predict similar values for most of the observables listed in table 7. We now have two contributions from the PDR and the shocks and for each quantity listed in table 7 we quote in brackets which fraction comes from the shocks. The weight of the PDR model in both best solutions is slightly different, and this yields a mass-

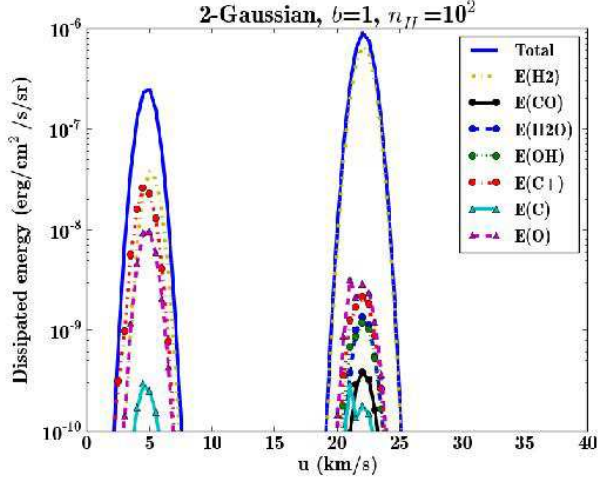


Figure 11. Distribution of the energy dissipated via several cooling agents for the 2-Gaussian best-fit model.

fraction of shocked matter on the line of sight of 4% in the piecewise-exponential model and 19% in the 2-Gaussians model. The contribution from shocks is hence small but not insignificant. However, molecules other than H₂ are all formed in the shocks and not in the PDR, with for example 98% of the CO coming from the shocks. Note that in both our two best models, shocks with velocity above 15 km.s⁻¹ account for the formation of almost all molecules. This is due to the overcome of chemical barriers thanks to the thermal energy released in shocks and to the ion-neutrals drift, as mentioned in sections 3.4 and 3.5.

CH⁺ needs mechanical energy injection to raise the **effective** temperature for its formation which is why pure PDR models failed to account for its abundance. In fact, CH⁺ forces a too hot component into the model, which then over-produces the $J = 5$ H₂-level. A possible solution would be that the irradiation in the far-UV is enhanced in the Chamaeleon compared to the Draine ISRF: this would make more CH⁺ from CH₂⁺ and CH₃⁺ photo-dissociation (Falgarone et al. 2010) while requiring a lower temperature more compatible with the observed $J = 5$ H₂-level column-density. In fact, UV spectra in Boulanger et al. (1994) suggest that the enhanced far-UV field could be accounted by a flatter extinction curve in the far-UV for this very line of sight.

As for the SQ, H₂ is by far the main cooling agent (it radiates more than 92% of the total cooling in both best-fit models) but CII (and OI to a lesser extent) has emission comparable to the H₂-S(1) line. Even though it is now dominated by the emission from the PDR, the shock contribution to CII emission is still significant (from 18% to 31% according to both best models). Interestingly, we predict OH should shine about as much as CII and as for the SQ solution, the OH emission is almost completely dominated by the contribution from shocks at moderate velocity. OH observations would hence provide a good test of the existence or not of a moderate velocity shock component in the Chamaeleon.

| names | piecewise-exp | 2-Gaussian | obs | error | SQ shock) |
|---|---------------|------------|---------|--------|---|
| Column-densities (cm^{-2}) | | | | | combination of shock models as a phenomenological description of the complex statistical properties of the dissipation of turbulence. The model provides a rather good match to the data for bimodal distributions of shock velocities. This does not match predictions from numerical simulations of Smith et al. (2000) who found a power-law distribution with an exponential cut-off. Further work is needed to understand the reasons behind this apparent discrepancy. Interestingly, the low and moderate velocity components of our best-fit PDF operate in very different regimes of energy dissipation. Indeed, in our best-fit models to the observations, the low velocity shocks are of C-type and they dissipate energy via ion-neutral drift whereas the larger velocity shocks are of J-type and they undergo viscous dissipation. In both our interpretations of the SQ and the Chamaeleon, a significant fraction of the molecular gas is shock heated and the chemistry in this shock heated gas has a dominant contribution to key molecules such as CO, H ₂ O, OH or CH ⁺ which are commonly used as diagnostics. This shock heated contribution might be greater than the contribution of CO computed in simulations by Glover & Mac Low (2011) where the resolution in the shocks is too scarce to trigger the shock chemistry: too low resolution smears out the temperature to such an extent that shocks become nearly isothermal with a temperature too low for molecule formation. Furthermore, although low-velocity shocks are less efficient than moderate velocity shocks, they are more numerous and depending on the statistical distribution of shocks they could potentially account for a higher fraction of the excitation and formation of molecules. |
| Observations | | | | | |
| N(H) | 2.6(20) | [0.06] | 2.7(20) | [0.23] | 3.1(20) |
| H ₂ (0,0) | 1.8(20) | [0.04] | 1.8(20) | [0.20] | 2.0(20) |
| H ₂ (0,1) | 2.1(20) | [0.03] | 1.9(20) | [0.14] | 1.4(20) |
| H ₂ (0,2) | 2.6(18) | [0.53] | 2.6(18) | [0.61] | 2.6(18) |
| H ₂ (0,3) | 4.2(17) | [0.99] | 4.9(17) | [0.99] | 2.0(17) |
| H ₂ (0,4) | 4.4(16) | [1.00] | 5.9(16) | [1.00] | 2.0(16) |
| H ₂ (0,5) | 2.2(16) | [1.00] | 3.8(16) | [1.00] | 7.1(14) |
| N(C) | 2.4(15) | [0.20] | 2.3(15) | [0.30] | 6.0(14) |
| N(CO) | 5.2(13) | [0.98] | 4.9(13) | [0.98] | 5.6(13) |
| N(CH) | 6.2(12) | [0.87] | 4.8(12) | [0.86] | 6.4(12) |
| N(CH ⁺) | 8.8(12) | [1.00] | 1.0(13) | [1.00] | 1.2(13) |
| Predictions | | | | | |
| N(H ₂) | 3.9(20) | [0.04] | 3.8(20) | [0.17] | - |
| N(C ⁺) | 1.4(17) | [0.05] | 1.4(17) | [0.19] | - |
| N(H ₂ O) | 2.8(13) | [0.99] | 5.3(13) | [1.00] | - |
| N(OH) | 6.9(13) | [0.99] | 1.1(14) | [0.99] | - |
| N(HCO ⁺) | 2.7(11) | [0.99] | 3.4(11) | [0.99] | - |
| N(CN) | 3.9(11) | [0.99] | 5.3(11) | [0.99] | <5.9(11) |
| N(C ₂) | 3.6(10) | [0.80] | 2.8(10) | [0.77] | <1.4(13) |
| Atomic lines ($\text{erg.cm}^{-2}.\text{s}^{-1}.\text{sr}^{-2}$) | | | | | |
| S(25.2m) | 4.5(-9) | [1.00] | 5.1(-9) | [1.00] | - |
| Si+(34.8m) | 6.4(-8) | [0.82] | 6.0(-8) | [0.84] | - |
| O(63.2m) | 1.2(-6) | [0.66] | 1.1(-6) | [0.67] | - |
| O(145.3m) | 8.7(-8) | [0.76] | 7.7(-8) | [0.77] | - |
| C+(158m) | 3.8(-6) | [0.18] | 3.9(-6) | [0.31] | 2.8(-6) |
| C(370.4m) | 2.2(-8) | [0.60] | 2.3(-8) | [0.68] | - |
| C(609.8m) | 1.3(-8) | [0.33] | 1.3(-8) | [0.44] | - |
| Molecular cooling ($\text{erg.cm}^{-2}.\text{s}^{-1}.\text{sr}^{-1}$) | | | | | |
| 0-0S(1) | 1.9(-6) | [0.99] | 2.2(-6) | [0.99] | - |
| E(H ₂) | 9.5(-5) | [1.00] | 5.7(-5) | [0.99] | - |
| E(CO) | 9.3(-8) | [1.00] | 8.5(-8) | [1.00] | - |
| E(H ₂ O) | 1.8(-7) | [1.00] | 2.3(-7) | [1.00] | - |
| E(OH) | 2.9(-6) | [1.00] | 2.0(-6) | [1.00] | - |

Table 7. Results and predictions of the fit of piecewise-exponential to the Chamaeleon data (Gry et al. 2002; Nehmé et al. 2008). **Powers of ten are indicated in parentheses.** For each value, we provide the fraction coming from the shocks in brackets.

5. Summary, conclusions, discussion, prospects

We provide to the scientific community a grid of shock models³ in UV heated gas which may be used to interpret observations of the Milky-Way diffuse ISM and integrated properties of galaxies in general. We examine magnetised shocks in media with densities from $n_{\text{H}} = 10^2$ to 10^4 cm^{-3} , with standard ISM irradiation conditions and at low to moderate velocities (from 3 to 40 km.s^{-1}). When the velocity of these shocks is below the critical velocity for the existence of pure C-type shocks, we compute C-type shocks, otherwise, we compute J-type shocks. The models include the effects of the ambient UV irradiation field on the pre-shock chemistry and thereby on the relative importance of cooling lines in the shock. For instance, C⁺ can provide significant line cooling in shocks propagating in the UV irradiated gas where it is the dominant carbon species.

We illustrate how the model results may be used to interpret data on one galactic line of sight through the diffuse ISM (Chamaeleon) and one extra-galactic object (the

³ The output data of our models is archived on <http://cemag.ens.fr>

with an effective transfer back to kinetic energy. Thus, shocks are actors which contribute to the equipartition between various forms of energy, thanks to a continuous recycling of the gas throughout successive shock structures.

The main caveat of our study is that we assume the relaxation of the post-shock pressure takes place instantaneously: namely, our model accounts for the pre-shock gas and the shocked gas but does not incorporate the expansion of the gas after the shock. We shall attempt to model this phase in future studies. **Another caveat of our study lies in the implicit assumption that all shocks are steady. Indeed some shock velocities are prone to instabilities and even quasi-steady models are invalid in this case (see Lesaffre et al. 2004b, for example).** Less important caveats are the shock orientation, its curvature, the neglect of intermediate ages of shocks (for ages lower than about 10^4 yr, we should consider CJ-type shocks or non-steady shocks). We believe that these minor caveats are washed out by the fact that we fit a statistical collection of shock velocities. Finally we do not treat UV pumping in the H_2 -population but Monteiro et al. (1988) showed this starts to make a difference only for H_2 levels above $J = 5$ and for $G_0 \gg 1$.

Our PDF fitting technique might prove useful to account for single shocks with more complicated geometries. For example, a single bow-shock effectively encompasses a continuous collection of velocities depending on the angle at which each fluid parcel of pre-shock gas impinges on the bow-shock. In such a framework, the shape of the lines is directly related to the dynamics inside the shock, and not simply due to the relative motions between each shocks as in the statistical distribution of shocks we infer in the SQ. In such cases, it will therefore be interesting to predict and use the line shapes as additional observational constraints on the shock physics.

Finally, as we already mentioned, the dissipation of turbulent motions does not occur only in shocks. It will be interesting in future work to assess on the one hand what fraction of the energy dissipation takes place in vortices, current sheets or shocks, for example. On the other hand, it will be worth comparing vortex models as in Godard et al. (2009) to our own shock models in order to check whether we can disentangle observationally the respective signatures of shocks and vortices.

Acknowledgements. P.L., E.F. and B.G. acknowledge support from SCHISM A.N.R.. We thank Maryonne Gerin and Antoine Gusdorf for comments on the manuscript. We thank the anonymous referee for his comments which improved the readability of the paper.

References

- Abrahamsson, E., Krems, R. V., & Dalgarno, A. 2007, ApJ, 654, 1171
 Agúndez, M., Goicoechea, J. R., Cernicharo, J., Faure, A., & Roueff, E. 2010, ApJ, 713, 662
 Appleton, P. N., Xu, K. C., Reach, W., et al. 2006, ApJ, 639, L51
 Audit, E. & Hennebelle, P. 2005, A&A, 433, 1
 Audit, E. & Hennebelle, P. 2010, A&A, 511, A76+
 Bergin, E. A., Hartmann, L. W., Raymond, J. C., & Ballesteros-Paredes, J. 2004, ApJ, 612, 921
 Black, J. H. & van Dishoeck, E. F. 1987, ApJ, 322, 412
 Boulanger, F., Prevot, M. L., & Gry, C. 1994, A&A, 284, 956
 Chièze, J.-P., Pineau des Forêts, G., & Flower, D. R. 1998, MNRAS, 295, 672
 Cluver, M. E., Appleton, P. N., Boulanger, F., et al. 2010, ApJ, 710, 248
 Crutcher, R. M., Wandelt, B., Heiles, C., Falgarone, E., & Troland, T. H. 2010, ApJ, 725, 466
 Draine, B. T. 1978, ApJS, 36, 595
 Draine, B. T. 1980, ApJ, 241, 1021
 Draine, B. T. & Bertoldi, F. 1996, ApJ, 468, 269
 Draine, B. T., Roberge, W. G., & Dalgarno, A. 1983, ApJ, 264, 485
 Falgarone, E., Hily-Blant, P., Pety, J., & Pineau des Forêts, G. 2007, in IAU Symposium, Vol. 237, IAU Symposium, ed. B. G. Elmegreen & J. Palous, 24–30
 Falgarone, E., Ossenkopf, V., Gerin, M., et al. 2010, A&A, 518, L118
 Falgarone, E., Verstraete, L., Pineau des Forêts, G., & Hily-Blant, P. 2005, A&A, 433, 997
 Flower, D. R., Le Bourlot, J., Pineau des Forêts, G., & Cabrit, S. 2003, MNRAS, 341, 70
 Flower, D. R. & Pineau des Forêts, G. 2003, MNRAS, 343, 390
 Flower, D. R. & Pineau des Forêts, G. 2010, MNRAS, 406, 1745
 Flower, D. R., Pineau des Forêts, G., & Hartquist, T. W. 1985, MNRAS, 216, 775
 Flower, D. R., Pineau-des-Forêts, G., & Hartquist, T. W. 1986, MNRAS, 218, 729
 Gerlich, D., Disch, R., & Scherbarth, S. 1987, J. Chem. Phys., 87, 350
 Glover, S. C. O. & Mac Low, M.-M. 2011, MNRAS, 412, 337
 Godard, B., Falgarone, E., Gerin, M., et al. 2012, A&A, 540, A87
 Godard, B., Falgarone, E., & Pineau des Forêts, G. 2009, A&A, 495, 847
 Gredel, R., Pineau des Forêts, G., & Federman, S. R. 2002, A&A, 389, 993
 Gry, C., Boulanger, F., Nehmé, C., et al. 2002, A&A, 391, 675
 Guillard, P., Boulanger, F., Cluver, M. E., et al. 2010, A&A, 518, A59+
 Guillard, P., Boulanger, F., Pineau des Forêts, G., & Appleton, P. N. 2009, A&A, 502, 515
 Guillard, P., Boulanger, F., Pineau des Forêts, G., et al. 2012, ApJ, 749, 158
 Guillet, V., Pineau des Forêts, G., & Jones, A. P. 2007, A&A, 476, 263
 Heck, L., Flower, D. R., & Pineau des Forêts, G. 1990, Computer Physics Communications, 58, 169
 Hennebelle, P. & Audit, E. 2007, A&A, 465, 431
 Hierl, P. M., Morris, R. A., & Viggiano, A. A. 1997, J. Chem. Phys., 106, 10145
 Hollenbach, D. & McKee, C. F. 1989, ApJ, 342, 306
 Ingalls, J. G., Bania, T. M., Boulanger, F., et al. 2011, ApJ, 743, 174
 Jenkins, E. B. 2009, ApJ, 700, 1299
 Koyama, H. & Inutsuka, S.-i. 2002, ApJ, 564, L97
 Le Petit, F., Nehmé, C., Le Bourlot, J., & Roueff, E. 2006, ApJS, 164, 506
 Lee, H.-H., Herbst, E., Pineau des Forêts, G., Roueff, E., & Le Bourlot, J. 1996, A&A, 311, 690
 Lesaffre, P., Chièze, J.-P., Cabrit, S., & Pineau des Forêts, G. 2004a, A&A, 427, 147
 Lesaffre, P., Chièze, J.-P., Cabrit, S., & Pineau des Forêts, G. 2004b, A&A, 427, 157
 Monchick, L. & Schaefer, J. 1980, J. Chem. Phys., 73, 6153
 Monteiro, T. S., Flower, D. R., Pineau des Forêts, G., & Roueff, E. 1988, MNRAS, 234, 863
 Mouri, H., Hori, A., & Takaoka, M. 2008, Physics of Fluids, 20, 035108
 Mullan, D. J. 1971, MNRAS, 153, 145
 Nehmé, C., Le Bourlot, J., Boulanger, F., Pineau des Forêts, G., & Gry, C. 2008, A&A, 483, 485
 Neufeld, D. A. & Kaufman, M. J. 1993, ApJ, 418, 263
 Pety, J. & Falgarone, E. 2000, A&A, 356, 279
 Pineau des Forêts, G., Flower, D. R., Hartquist, T. W., & Dalgarno, A. 1986, MNRAS, 220, 801
 Roberge, W. G. & Draine, B. T. 1990, ApJ, 350, 700
 Smith, M. D., Mac Low, M.-M., & Heitsch, F. 2000, A&A, 362, 333
 Suzuki, T., Kaneda, H., Onaka, T., & Kitayama, T. 2011, ApJ, 731, L12
 Wardle, M. 1998, MNRAS, 298, 507
 Wyrowski, F., van der Tak, F., Herpin, F., et al. 2010, A&A, 521, L34